3D cloud tomography and droplet size retrieval from multi-angle polarimetric imaging of scattered sunlight from above

Aviad Levis[a], Anthony B. Davis[b], Jesse R. Loveridge[c], and Yoav Y. Schechner[d]

[a] Computer & Mathematical Sciences Department, California Institute of Technology, Pasadena, CA, 91125, USA
[b] Jet Propulsion Laboratory, California Institute of Technology, Mail Stop 233 - 200, Pasadena, CA, 91109, USA
[c] Department of Atmospheric Sciences, University of Illinois - Urbana Champaign, Champaign, IL, 61820, USA
[d] Viterbi Faculty of Electrical Engineering, Technion – Israel Institute of Technology, Haifa, 3200003, Israel

ABSTRACT

Tomography aims to recover a three-dimensional (3D) density map of a medium or an object. In medical imaging, it is extensively used for diagnostics via X-ray computed tomography (CT). We define and derive a tomography of cloud droplet distributions via passive remote sensing. We use multi-view polarimetric images to fit a 3D polarized radiative transfer (RT) forward model. Our motivation is 3D volumetric probing of vertically-developed convectively-driven clouds that are ill-served by current methods in operational passive remote sensing. Current techniques are indeed based on strictly 1D RT modeling and applied to a single cloudy pixel, where cloud geometry defaults to that of a plane-parallel slab. Incident unpolarized sunlight, once scattered by cloud droplets, changes its polarization state according to droplet size. Therefore, polarimetric measurements in the rainbow and glory angular regions can be used to infer the droplet size distribution. This work defines and derives a framework for a full 3D tomography of cloud droplets for both their mass concentration in space and their distribution across a range of sizes. This gridded 3D retrieval of key microphysical properties is made tractable by our novel approach that involves a restructuring and partial linearization of an open-source polarized 3D RT code to accommodate a special two-step iterative optimization technique. Physically-realistic synthetic clouds are used to demonstrate the methodology with rigorous uncertainty quantification, while a real-world cloud imaged by AirMSPI is processed to illustrate the new remote sensing capability.

Keywords: polarization, 3D vector radiative transfer, inverse problems, tomography, remote sensing, convective clouds, cloud microphysics, aerosol plumes, AirMSPI

1. MOTIVATION, CONTEXT & OUTLINE

Clouds play a significant role at local and global scales, affecting weather, the water cycle, solar power generation, and impacting Earth's energy balance.[1] Moreover, uncertainties in global climate models are significantly affected by our limited understanding, and therefore modeling, of cloud dynamics and microphysics.[2] Thus, understanding, modeling, and predicting cloud properties is a key issue with worldwide socio-economic implications that is in the center of many research studies.[3] Much of the current understanding relies on routine remote sensing of cloud properties such as by the MODerate resolution Imaging Spectrometer (MODIS).[4] In practice, global-scale retrievals have so far been based on an individual pixel basis, using a crude approximation that clouds are plane-parallel slabs. This approximation uses a 1D radiative transfer (RT) model, which leads to biases in many retrievals[5] while other retrievals simply fail.[6] Convective clouds are therefore a blind spot due to their
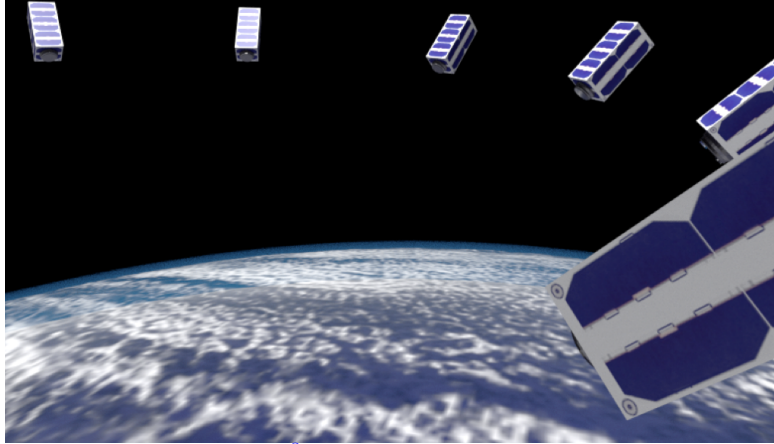
Figure 1: Artist's illustration of the CloudCT[8] mission: a distributed multi-view system of 10 nano-satellites orbiting the Earth in formation. Measurements acquired by the formation will enable tomographic retrievals of cloud properties.

inherently 3D nature. In its 2018 *Decadal Strategy for Earth Observation from Space*,[7] the National Academies of Sciences, Engineering, and Medicine have indeed identified "Clouds, Convection, and Precipitation" as one of its five top-priority Targeted Variables for NASA's next generation of satellite missions. To bridge this gap, new technology is needed to study clouds as 3D volumetric objects, on a global scale. The *CloudCT*[8] space mission, funded by the European Research Council (ERC) is specifically designed to provide data and products for this goal. It will involve 10 nano-satellites orbiting in formation, thus acquiring simultaneously unique multi-view measurements of such vertically-developed 3D clouds (Fig. 1).

Moreover, common retrieval of cloud droplet characteristics use two optical bands simultaneously:[9] a visible band, where reflected radiance increases with cloud optical thickness, and a shortwave IR (SWIR) band, where absorption by condensed water depends on cloud droplet size. To sense droplet size in 3D by CloudCT or other future missions, sensors will need to have either SWIR or polarization capability.

1.1 Why polarized light?

There is an additional caveat in common retrievals, which rely on SWIR absorption.[9] In addition to absorption, light undergoes multiple scattering in clouds. Multiple scattering diminishes sensitivity to droplet microphysics. High sensitivity to microphysics is embedded in single-scattering events. It is thus beneficial to pick-up single-scatter signals, out of the strong multiply-scattered background radiance. Polarization signals of scattered light are dominated by single-scattering events, and are thus highly sensitive to the type and size specifications of scatters. Thus in recent years, there is growing interest in polarimetric imagers for remote sensing of clouds and aerosols.[10–15] In turn, increased interest in polarimetric sensing capabilities has led to the development of 1D[16] and 3D[17] polarized (or "vector") RT codes with an aim of improving retrieval algorithms. Motivated by the CloudCT mission formulation—only the first of many to come in innovative passive cloud remote sensing—we have recently developed a novel framework for 3D remote sensing of cloud properties using multi-view polarimetric measurements.[18] That research is summarized and augmented in the following.

1.2 Why passive tomography?

From its etymology, the word "tomography" means a slice-by-slice recovery of an object's 3D internal structure using 2D projections of cumulative density. In the computer age, this task is termed *Computed Tomography* (CT) .[19] Common medical CT approaches are transmission-based X-ray CT or single-photon emission computed tomography (SPECT). There, 2D projections represent straight line-of-sight (LOS) integrals of the local X-ray opacity or nuclear marker density, respectively. In both imaging modalities, the inverse problem of recovering the medium content is *linear*.[20] Biomedical imaging also involves CT modalities that are not based on linear

projections. A prime example is Optical Diffusion Tomography (ODT),[21–23] which uses non-ionizing near-infrared light.[*]

Rather than ODT's time-dependent 3D photon diffusion model, we use a steady-state polarized 3D RT forward model to compute remote sensing observations for a given cloud scene. Specifically, we adopt *vector* Spherical Harmonics Discrete Ordinates Method (vSHDOM),[25, 26] a popular computational 3D polarized RT model that, importantly here, is open source. We then formulate an inverse 3D RT problem for cloud tomography utilizing multi-view multi-spectral polarimetric images. In contrast to linear CT, the image formation model is nonlinear in the cloud's microphysical and density variables. Our approach seeks an optimal fit of droplet microphysical and density parameters by generalizing our two-step iterative inversion approach, already demonstrated on intensity-only observations,[27–29] to take advantage of polarimetric measurements.

To the best of our knowledge, only Martin et al.[30] have at least formulated a potentially very efficient atmosphere/surface tomography based on the *adjoint* 3D vector RT equation. The method was demonstrated convincingly on a 2D cloud extinction field,[31] however, it was done with intensity data only.

1.3 Outline

In the next section, we cover basic cloud droplet optics using Mie scattering theory and the fundamentals of polarized 3D RT. The latter yields radiance, which has a clear decomposition into single- and multiply-scattered light. This decomposition supports the solution to the inverse problem at hand. In Section 3, we lay out our 3D cloud tomography method where we target three basic microphysical properties, volumetrically. Subsequently, the new 3D cloud tomographic capability is demonstrated in §4 on synthetic but realistic clouds from an LES that provide ground truth for rigorous retrieval error quantification. That proof-of-concept is followed by an illustration with real-world data processing described in §5. Finally, we conclude in §6 with a summary and an outline of future developments, mostly looking toward CloudCT and other space-based uses.

2. THEORETICAL BACKGROUND

This section describes bulk microphysical parameterization of scattering media, the polarimetric radiative transfer image formation (forward) model, and the relation between them. The section also describes the coordinate systems in use (per-scatterer, imager and Earth frames). We further decompose the polarized radiance into single-scattered and high-order scattered components. These foundations are used in subsequent sections, to formulate tomographic recovery.

2.1 Scatterer microphysical properties

In the lower atmosphere, cloud particles are droplets of liquid water that are very nearly spherical, having radius r. They are however polydisperse, with a droplet size distribution denoted $n(r)$. For most remote-sensing purposes, $n(r)$ is parameterized using an *effective radius* in μm and a dimensionless *variance*:[32]

$$r_{\mathrm{e}} = \frac{\int_0^\infty r^3 n(r)\mathrm{d}r}{\int_0^\infty r^2 n(r)\mathrm{d}r}, \quad v_{\mathrm{e}} = \frac{\int_0^\infty (r-r_{\mathrm{e}})^2 r^2 n(r)\mathrm{d}r}{r_{\mathrm{e}}^2 \int_0^\infty r^2 n(r)\mathrm{d}r}. \tag{1}$$

A commonly used parametric size distribution, having empirical support[32] is the *Gamma*-distribution (Fig. 2):

$$n(r) = N\, c\, r^{(v_{\mathrm{e}}^{-1}-3)} \exp[-r/(r_{\mathrm{e}} v_{\mathrm{e}})], \tag{2}$$

where we require $v_{\mathrm{e}} < 1/2$. Here $c = (r_{\mathrm{e}} v_{\mathrm{e}})^{(2-v_{\mathrm{e}}^{-1})}/\Gamma(v_{\mathrm{e}}^{-1}-2)$ is a normalization constant and

$$N = \int_0^\infty n(r)\mathrm{d}r \tag{3}$$

---

[*]The work by Che et al.[24] is noteworthy in that departs from physics-based approaches into the realm of machine learning.
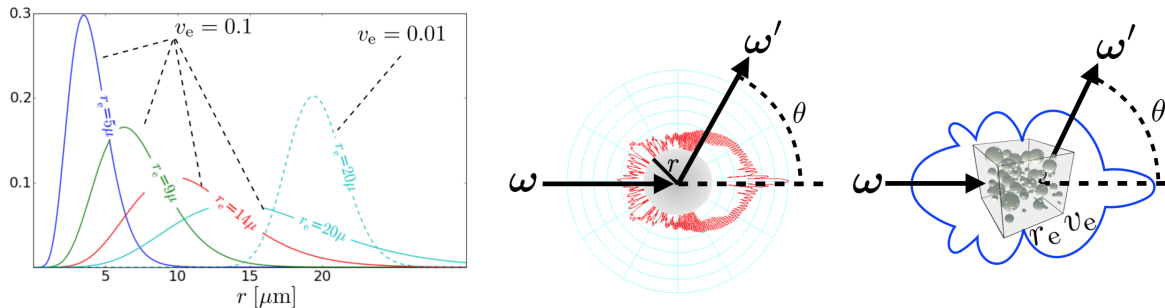
Figure 2: [Left] Normalized *Gamma*-distribution. The effective radius and variance dictate the centroid and width of the size-distribution. The limit of very low v_e approaches a mono-disperse distribution. [Center] Log-polar plot of the Mie phase-function p_{11} induced by a single water sphere of radius r. [Right] Log-polar plot of the effective phase-function $\langle s_s p_{11}\rangle_r / \sigma_s$ induced by a small volume that includes particles of different sizes.

is the droplet number concentration. Let ρ_w be the density of liquid water. An important cloud characteristic is the water mass density or liquid water content (LWC) per unit volume:

$$\text{LWC} = \frac{4}{3}\pi\rho_w \int_0^\infty r^3 n(r)\mathrm{d}r. \tag{4}$$

It is expressed as $\text{LWC} = {}^{4}\!/\!_3\, \pi\rho_w r_e^3(1-v_e)(1-2v_e)$ for the Gamma distribution in (2).

2.2 Polarized light

It is convenient to define the polarized light state in terms of the Stokes[32] vector $\mathbf{I} = (I, Q, U, V)^\top$. I is non-polarized or total intensity. The degrees of polarization (DOP) and linear polarization (DoLP) are respectively defined as the ratios $\sqrt{Q^2+U^2+V^2}/I$, $\sqrt{Q^2+U^2}/I$. The angle of linear polarization (AoLP) is ${}^{1}\!/\!_2 \tan^{-1}(U/Q)$.

2.3 Single scattering of polarized light

Light interaction with a single particle is described by the total extinction cross-section $s_t(r,\lambda)$, decomposed into scattering and absorption cross-sections, respectively:

$$s_t(r,\lambda) = s_s(r,\lambda) + s_a(r,\lambda). \tag{5}$$

In Mie-Lorentz scattering by spheres, which is introduced further on, we have

$$s_t(r,\lambda) = \pi\, r^2\, \mathcal{Q}t(2\pi\, r/\lambda), \quad s_s(r,\lambda) = \pi\, r^2\, \mathcal{Q}s(2\pi\, r/\lambda), \quad s_a(r,\lambda) = \pi\, r^2\, \mathcal{Q}a(2\pi\, r/\lambda)$$

where $\mathcal{Q}t, \mathcal{Q}s, \mathcal{Q}a$ are dimensionless efficiency factors that depend only on the normalized size parameter $2\pi\, r/\lambda$. In the limit $r \gg \lambda$, $\mathcal{Q}t \approx 2$. Furthermore, when $s_s(r,\lambda) \gg s_a(r,\lambda)$, then $\mathcal{Q}s \approx 2$ and $\mathcal{Q}a \approx 0$.

Define size-weighted average over a function $a(r)$ by

$$\langle a \rangle_r = \frac{1}{N}\int_0^\infty a(r)n(r)\mathrm{d}r. \tag{6}$$

Note that we use here an approximation, commonly used in multi-spectral remote sensing, of a single rendering with spectrally-averaged optical properties. The material optical properties can furthermore be approximated, in the absence of molecular absorption, by using a single wavelength for each spectral band. This is valid if wavelength dependencies within a spectral band are weak, a condition met when narrow bands are considered. Macroscopic optical cross-sections are then expressed as weighted averages[†]

$$\sigma_t(\lambda) = \langle s_t(r,\lambda)\rangle_r, \ \sigma_s(\lambda) = \langle s_s(r,\lambda)\rangle_r, \ \sigma_a(\lambda) = \langle s_a(r,\lambda)\rangle_r. \tag{7}$$

[†]Aggregating scattered properties in (7) rather than electric fields holds for scatterer populations that are in each other's far field (i.e., are $\gg \lambda$ apart).[32]

Throughout the text, dependency on λ is generally omitted for simplicity; however, it is used at specific points as needed.

Scattering, as a fraction of the overall interaction, is expressed by the dimensionless *single scattering albedo*

$$\varpi = \frac{\sigma_s}{\sigma_t}. \tag{8}$$

The extinction coefficient (or optical density) is denoted by β. Following Eqs. (3), (4) and (7), $\beta = N\sigma_t$ is expressed in terms of the LWC as[33]

$$\beta = \frac{\text{LWC}}{\frac{4}{3}\pi\rho_w\langle r^3\rangle_r}\sigma_t = \text{LWC}\cdot\tilde{\sigma}_t. \tag{9}$$

Here, $\tilde{\sigma}_t$ is the mass extinction coefficient (in units of $^{m^2}/_g$).

Let $\boldsymbol{\omega}$ and $\boldsymbol{\omega}'$ be the unitary incident and scattered ray direction vectors respectively in Fig. 2. Single-scattering geometry is defined by the local coordinate system of the incoming beam's electric fields. The scattering angle is $\theta = \cos^{-1}(\boldsymbol{\omega}\cdot\boldsymbol{\omega}')$. The angular redistribution of singly-scattering light from a sphere of is defined by the 4×4 dimensionless *Mueller* matrix $\mathbf{P}_s(\theta, r)$. The macroscopic *phase matrix* is the size-weighted average

$$\mathbf{P}(\theta) = \frac{\langle s_s(r)\mathbf{P}_s(\theta, r)\rangle_r}{\sigma_s}. \tag{10}$$

For spherical (or just randomly-oriented) particles, the phase-matrix $\mathbf{P}(\theta)$ takes the following symmetric form[32]

$$\mathbf{P}(\theta) = \begin{bmatrix} p_{11}(\theta) & p_{21}(\theta) & 0 & 0 \\ p_{21}(\theta) & p_{22}(\theta) & 0 & 0 \\ 0 & 0 & p_{33}(\theta) & -p_{43}(\theta) \\ 0 & 0 & p_{43}(\theta) & p_{44}(\theta) \end{bmatrix}, \tag{11}$$

where p_{11} is the (unpolarized) scattering phase-function. In single-scattering of unpolarized incident sunlight, the DoLP of scattered light amounts to the ratio $|p_{21}|/p_{11}$.

2.3.1 Rayleigh scattering

The Rayleigh model describes light scattering by particles much smaller than the wavelength. The Rayleigh phase matrix takes the following form[34]

$$\mathbf{P}_{\text{Rayl}}(\theta) = \begin{bmatrix} \frac{3}{4}\left(1+\cos^2\theta\right) & -\frac{3}{4}\sin^2\theta & 0 & 0 \\ -\frac{3}{4}\sin^2\theta & \frac{3}{4}\left(1+\cos^2\theta\right) & 0 & 0 \\ 0 & 0 & \frac{3}{2}\cos\theta & 0 \\ 0 & 0 & 0 & \frac{3}{2}\cos\theta \end{bmatrix}. \tag{12}$$

The single-scattering DoLP due to air molecules is then

$$\text{DoLP}_{\text{Rayl}}(\theta) = \frac{\sin^2\theta}{1+\cos^2\theta}. \tag{13}$$

According to (13), maximum DoLP is attained at single-scattering angle $\theta = 90°$.

2.3.2 Mie-Lorentz scattering

Mie-Lorentz scattering theory describes how light interacts with a spherical particle of size comparable to λ.[35] Denote $\mu = \cos\theta$. Mie-Lorentz scattering is defined in terms of complex-valued amplitude scattering functions $S_1(\mu), S_2(\mu)$. Scattering of the Stokes vector $\mathbf{I}$ is described by the phase matrix $\mathbf{P}_{\text{Mie}}(\mu)$, which is fully defined by four matrix components:

$$p_{11}^{\text{Mie}} = \frac{\varrho}{2}\left(S_1 S_1^* + S_2 S_2^*\right), \quad p_{12}^{\text{Mie}} = \frac{\varrho}{2}\left(S_1 S_1^* - S_2 S_2^*\right),$$
$$p_{33}^{\text{Mie}} = \frac{\varrho}{2}\left(S_1 S_2^* + S_2 S_1^*\right), \quad p_{43}^{\text{Mie}} = \frac{\varrho}{2}\left(S_1 S_2^* - S_2 S_1^*\right),$$
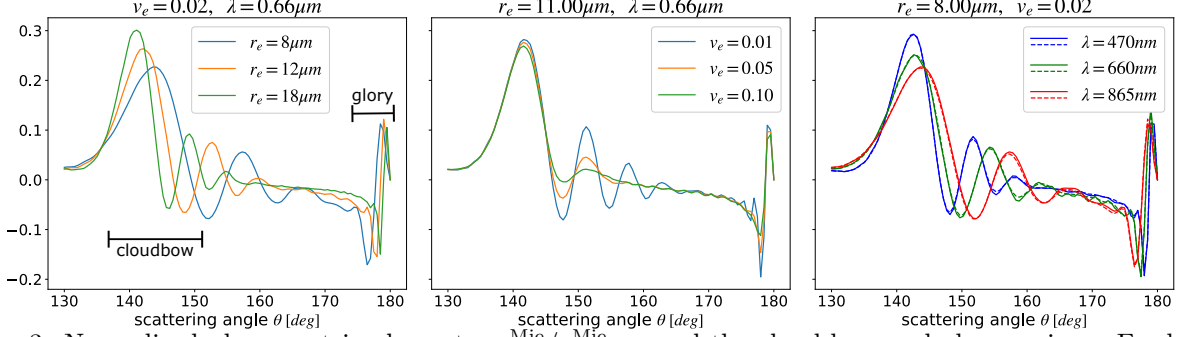
Figure 3: Normalized phase matrix element $-p_{12}^{\mathrm{Mie}}/p_{11}^{\mathrm{Mie}}$ around the cloud-bow and glory regions. For highly disperse droplet distributions (large v_e) the secondary lobes of the cloud-bow ($\theta \sim 140°$) and glory ($\theta \sim 180°$) diminish. The main cloud-bow peak is slightly sensitive to λ or v_e. [Left plot] The side-lobe angles are more sensitive to λ and r_e. [Middle plot] The side-lobe amplitude is sensitive to v_e. This cloud-bow signal is helpful for retrievals of r_e. [Right plot] Solid lines indicate monochromatic light. Dashed lines indicate spectral averaging over a 100 nm bandwidth, which is more than double any of the spectral bands considered further on.

with $p_{44}^{\mathrm{Mie}} = p_{33}^{\mathrm{Mie}}$ and $p_{22}^{\mathrm{Mie}} = p_{11}^{\mathrm{Mie}}$ in (11), while ϱ is a normalization constant, set to satisfy $\frac{1}{2}\int_{-1}^{1} p_{11}^{\mathrm{Mie}}(\mu)\mathrm{d}\mu = 1$.

Mie-Lorentz scattering due to water droplets is peaked at specific angles. For a single droplet (or monodisperse material), $\mathbf{P}^{\mathrm{Mie}}$ has sharp scattering lobes at angles that depend on the droplet's r/λ ratio. A macroscopic voxel contains droplets in a range of radii r, thus smoothing the scattering lobes. The smoothing effect depends on v_e (Fig. 3, middle) and, to a far lesser extent, the spectral bandwidth (Fig. 3, right) . Two angular domains that stand out for remote-sensing purposes are the cloud-bow ($\theta \in [135°, 155°]$) and glory ($\theta \in [175°, 180°]$). Both domains have peaks that are sensitive to the droplet microphysical parameters, and are significantly polarized (i.e., peaks are visible in the p_{12}^{Mie} component). The latter fact renders these peaks distinguishable in the presence of a multiply-scattered signal component.

2.4 Multiple scattering of polarized light

The radiative transfer equation (RTE)[34] describes multiple scattering interactions of monochromatic partially-polarized light within a medium. Transmittance between two points $\boldsymbol{x}_1, \boldsymbol{x}_2$ is

$$T\left(\boldsymbol{x}_1 {\to} \boldsymbol{x}_2\right) = \exp\left[-\int_{\boldsymbol{x}_1}^{\boldsymbol{x}_2} \beta(\boldsymbol{x})\mathrm{d}\boldsymbol{x}\right]. \tag{14}$$

An atmospheric domain Ω has boundary $\partial\Omega$. The intersection of $\partial\Omega$ with a ray originating at point $\boldsymbol{x}$ in direction $-\boldsymbol{\omega}$ (Fig. 4) is denoted $\boldsymbol{x}_0(\boldsymbol{x}, \omega)$. Denote the Stokes vector field as $\mathbf{I}(\boldsymbol{x}, \boldsymbol{\omega})$. Then $\mathbf{I}(\boldsymbol{x}_0, \boldsymbol{\omega})$ is the Stokes vector of radiation that propagates in direction $\boldsymbol{\omega}$ at boundary point $\boldsymbol{x}_0(\boldsymbol{x}, \boldsymbol{\omega})$. The non-emissive forward RT model[34] couples $\mathbf{I}(\boldsymbol{x}, \boldsymbol{\omega})$ to a vector *source field* $\mathbf{J}(\boldsymbol{x}, \boldsymbol{\omega})$ (Fig. 4) by

$$\mathbf{I}\left(\boldsymbol{x}, \boldsymbol{\omega}\right) = \mathbf{I}(\boldsymbol{x}_0, \boldsymbol{\omega})T\left(\boldsymbol{x}_0 {\to} \boldsymbol{x}\right) + \int_{\boldsymbol{x}_0}^{\boldsymbol{x}} \mathbf{J}(\boldsymbol{x}', \boldsymbol{\omega})\beta(\boldsymbol{x}')T\left(\boldsymbol{x}' {\to} \boldsymbol{x}\right)\mathrm{d}\boldsymbol{x}', \tag{15}$$

$$\mathbf{J}\left(\boldsymbol{x}, \boldsymbol{\omega}\right) = \frac{\varpi(\boldsymbol{x})}{4\pi} \int_{4\pi} \mathbf{P}\left(\boldsymbol{x}, \boldsymbol{\omega} {\cdot} \boldsymbol{\omega}'\right)\mathbf{I}\left(\boldsymbol{x}, \boldsymbol{\omega}'\right)\mathrm{d}\boldsymbol{\omega}'. \tag{16}$$

Equations (15)–(16) can be solved numerically, either directly with an explicit solver[26] or indirectly using a Monte-Carlo path tracer.[36] We use vSHDOM[26] to simulate scattered Stokes components of a realistic atmosphere, having both Mie-Lorentz and Rayleigh scattering due to water droplets and air molecules, respectively.

Sampling $\mathbf{I}(\boldsymbol{x}, \boldsymbol{\omega})$ at the location of each camera and direction of each camera pixel yields the measured Stokes vector. A measurement k is done at the camera position $\boldsymbol{x}_k$, LOS direction $\boldsymbol{\omega}_k$, and wavelength λ_k (Fig. 4). Thus, Eqs. (15)–(16) yield the pixel measurement model

$$\mathbf{I}[k] = \mathbf{I}\left(\boldsymbol{x}_0, \boldsymbol{\omega}_k\right)T\left(\boldsymbol{x}_0 {\to} \boldsymbol{x}_k\right) + \int_{\boldsymbol{x}_0}^{\boldsymbol{x}_k} \mathbf{J}\left(\boldsymbol{x}', \boldsymbol{\omega}_k\right)\beta(\boldsymbol{x}')T\left(\boldsymbol{x}' {\to} \boldsymbol{x}_k\right)\mathrm{d}\boldsymbol{x}'. \tag{17}$$
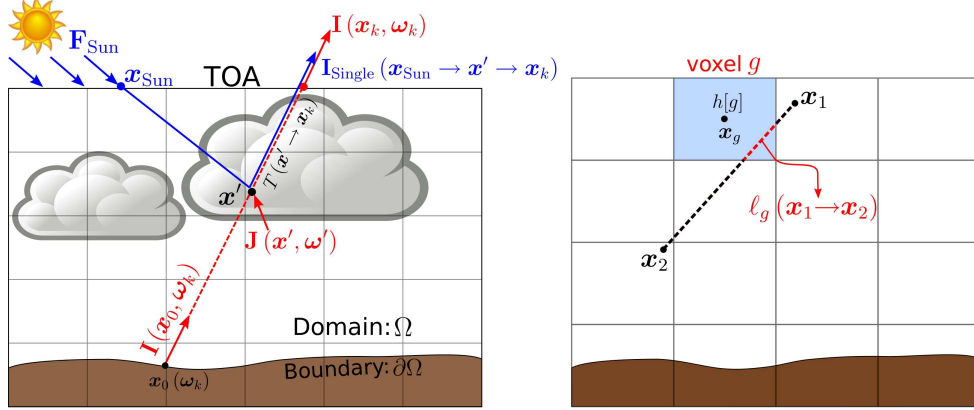
Figure 4: [Left] Light scatters in the medium, generally multiple times, creating a partially polarized (vector) scatter field $\mathbf{J}$ in Eq. (16). Integration yields the partially polarized (vector) light field $\mathbf{I}$ in Eq. (15). Here $I(\boldsymbol{x}_k, \boldsymbol{\omega}_k)$ is a pixel measurement at the TOA and $\mathbf{I}_{\mathrm{Single}}$ is the single-scattered contribution from $\boldsymbol{x}'$. [Right] Ray tracing of a line-integral over a discretized voxel field $h[g]$ (zero-order interpolation).

3. CLOUD TOMOGRAPHY

3.1 Inverse problem definition

So far, we have described the forward model, i.e., how images are formed, given cloud properties in 3D space, with a special emphasis on separating not only the directly transmitted but also the singly-scattered light from the diffuse light field. We can now formulate a novel inverse problem of recovering the unknown cloud microphysical properties, volumetrically, using tomographic techniques. In voxel g, the vector of unknown parameters is $(\mathrm{LWC}[g], \ r_{\mathrm{e}}[g], \ v_{\mathrm{e}}[g])$. The unknown microphysical parameters are concatenated to a vector of length $3N_{\mathrm{grid}}$

$$\boldsymbol{\Theta} = \left(..., \mathrm{LWC}[g], \ r_{\mathrm{e}}[g], \ v_{\mathrm{e}}[g], ...\right)^{\top}, \quad 1 \le g \le N_{\mathrm{grid}}. \tag{18}$$

Neglecting circular polarization, each pixel measures a Stokes vector, $\mathbf{y_I} = \left(y_I, y_Q, y_U\right)$ at N_λ wavelengths. Let N_{views} and N_{pix} denote the number of view points and camera pixels. The total number of Stokes measurements is thus $N_{\mathrm{meas}} = N_\lambda N_{\mathrm{views}} N_{\mathrm{pix}}$. The measurement vector of length $3N_{\mathrm{meas}}$ is expressed as

$$\mathbf{y} = \left(\mathbf{y_I}[1], ..., \mathbf{y_I}[N_{\mathrm{meas}}]\right)^{\top}. \tag{19}$$

In this section, we formulate the use of measurements $\mathbf{y}$ (multi-view, multi-pixel, multi-spectral, polarimetric measurements) for tomographic retrieval of $\boldsymbol{\Theta}$ (3D volumetric cloud density and microphysics).

3.2 Polarimetric information

To make an initial assessment of the sensitivity of polarimetric measurements, we simulate a simple homogeneous cubic cloud (Fig. 5), parameterized by two microphysical parameters: $(\mathrm{LWC}, r_{\mathrm{e}})$. Back-scattered Stokes measurements are taken at the TOA for angles and wavelengths as sampled by the Airborne Multi-angle Spectro-Polarimetric Imager (AirMSPI).[14] Define $I[k], U[k], Q[k]$ as simulated Stokes vector components at measurement index k. Define a cost function for each of the Stokes components

$$\mathcal{D}_{\mathrm{I}}\left(\mathrm{LWC}, r_{\mathrm{e}}\right) = \sum_{k=1}^{N_{\mathrm{meas}}} \left(I[k] - y_{\mathrm{I}}[k]\right)^2, \tag{20}$$

$$\mathcal{D}_{\mathrm{Q}}\left(\mathrm{LWC}, r_{\mathrm{e}}\right) = \sum_{k=1}^{N_{\mathrm{meas}}} \left(Q[k] - y_{\mathrm{Q}}[k]\right)^2, \tag{21}$$

$$\mathcal{D}_{\mathrm{U}}\left(\mathrm{LWC}, r_{\mathrm{e}}\right) = \sum_{k=1}^{N_{\mathrm{meas}}} \left(U[k] - y_{\mathrm{U}}[k]\right)^2, \tag{22}$$
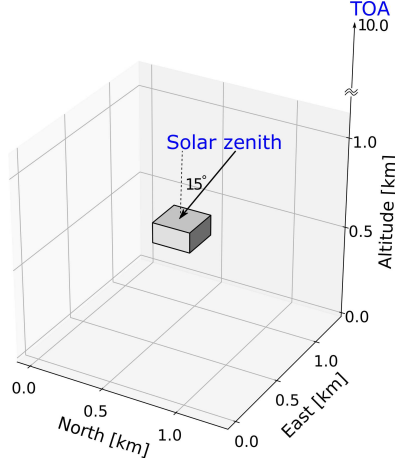
Figure 5: A homogeneous cubic cloud illuminated with solar radiation at a zenith angle of $15°$ off-nadir. The solar azimuth angles are $\phi_0 = [0.0°, 67.5°]$. The outgoing Stokes vector $\mathbf{I}$ is simulated at AirMSPI resolution and wavelengths, with AirMSPI measuring along a North-bound track.
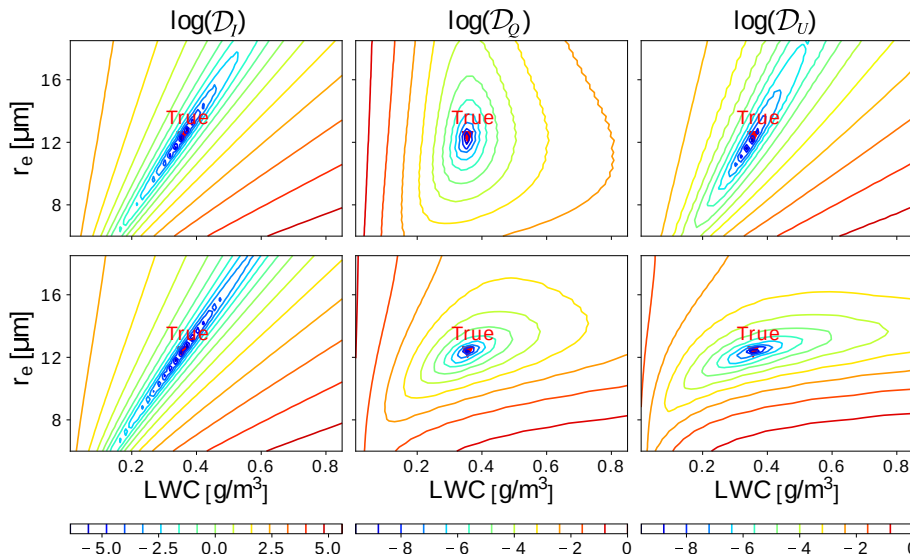

Figure 6: Logarithm of the 2D cost manifolds for the two-parameter homogeneous cubic cloud in Fig. 5. Each column of plots corresponds to the cost of the different Stokes components in Eqs. (20)–(22). Each row of plots corresponds to a different solar azimuth angle ϕ_0.

where we hold v_e constant. Equations (20)–(22) are 2D manifolds. Figure 6 plots the cost manifolds for different solar azimuth angles, ϕ_0. While there is an ambiguity between LWC and r_e when relying on $\mathcal{D}_I$, there are better defined minima for $\mathcal{D}_Q$ and $\mathcal{D}_U$. This indicates that polarization measurements carry valuable information.

4. SIMULATIONS

As previously mentioned, real data of simultaneous spaceborne multi-angular polarimetric images of clouds does not yet exist, but a mission to supply this data is in the works.[8] Therefore, we use careful simulations to test the approach. We simulate an atmosphere with molecular Rayleigh scattering and liquid water clouds. Rayleigh scattering is taken from the AFGL database[37] for a summer mid-latitude atmosphere. Mie tables are pre-computed for $r_e \in [4, 25]\,\mu$m and $v_e = 0.1$ with $N_{r_e} = 100$. The surface is Lambertian with a water-like albedo of 0.05.

For realistic complexity, a Large Eddy Simulation (LES) model[38] was used to generate a cloud field. Each voxel is of size $20{\times}20{\times}40\,\mathrm{m}^3$. The LES outputs[38] are clouds with 3D variable LWC and 1D (vertically) variable
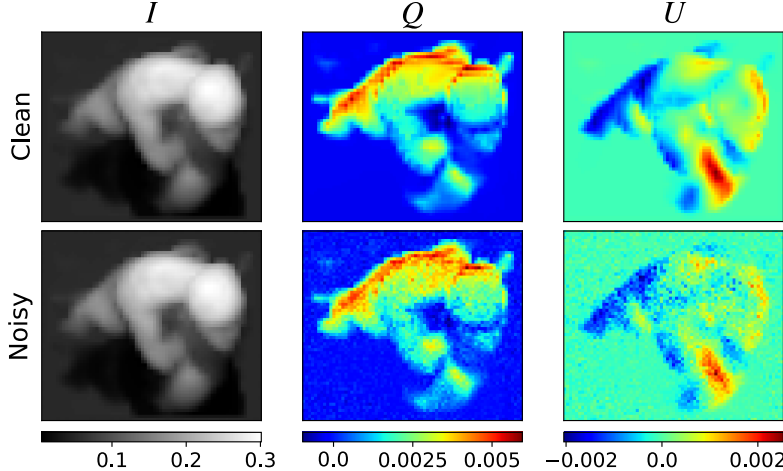
8

Figure 7: `Scene A` synthesized Stokes image using vSHDOM, before and after the application of a realistic AirMSPI noise model. We show here the *Bidrectional Reflectance Factor* (BRF) of the nadir view at λ=0.67μm.
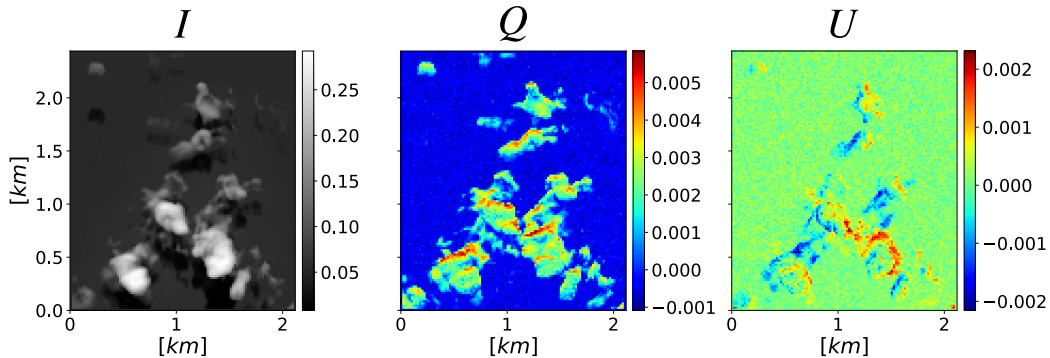

Figure 8: `Scene B` synthesized Stokes using vSHDOM. We show here the BRF of the nadir view at λ=0.67μm.

r_e. A typical value[39] of $v_\mathrm{e} = 0.1$ was chosen. Consequently, the present recovery demonstrations recover LWC and r_e on their respective native LES grid. However, $v_\mathrm{e} = 0.1$ is excluded for the moment from the unknowns.

From the generated cloud field, two isolated cloudy regions are taken for reconstruction:

1. `Scene A:` An atmospheric domain of dimensions $0.64{\times}0.72{\times}20$ km^3 with an isolated cloud (see synthetic AirMSPI nadir view in Fig. 7).

2. `Scene B:` An atmospheric domain of dimensions $2.42{\times}2.1{\times}8$ km^3 with several clouds of varying optical thickness (see synthetic AirMSPI nadir view in Fig. 8).

Synthetic measurements rendered with the spatial resolution and angular sampling of AirMSPI,[14] namely, 10 m pixels and 9 viewing angles: $\pm70.5°$, $\pm60°$, $\pm45.6°$, $\pm26.1°$, and $0°$ from zenith, where $\pm$ indicates fore- and aft-views along the northbound flight path. Solar zenith angle is $15°$ from nadir in the measurement plane, i.e., $0°$ solar azimuth. We simulate measurements at AirMSPI's three polarized spectral bands, namely, $\lambda = [0.47, 0.66, 0.865]$ μm. The bandwidths are narrow enough ($\approx$46 nm) to render images using a single representative wavelength per band.

Single scattering albedos for these wavelengths are all within 10^{-4} of unity. In other words, and in sharp contrast with the operational Nakajima–King[9] bi-spectral non-tomographic retrieval, absorption by droplets plays no role in this demonstration of tomography of cloud microphysics. The measurements are synthesized with realistic noise, according to the AirMSPI data acquisition model[40]) (see also Appendix C by Levis et al.[18]).

Qualitative volumetric results of the recovered LWC for `Scene A` are shown in Fig. 9. Scatter plot of the recovered LWC and the recovery results of r_e for `Scene A` are given in Fig. 10. Analogous plots for the larger `Scene B` recovery results can be found in Levis et al.[18]
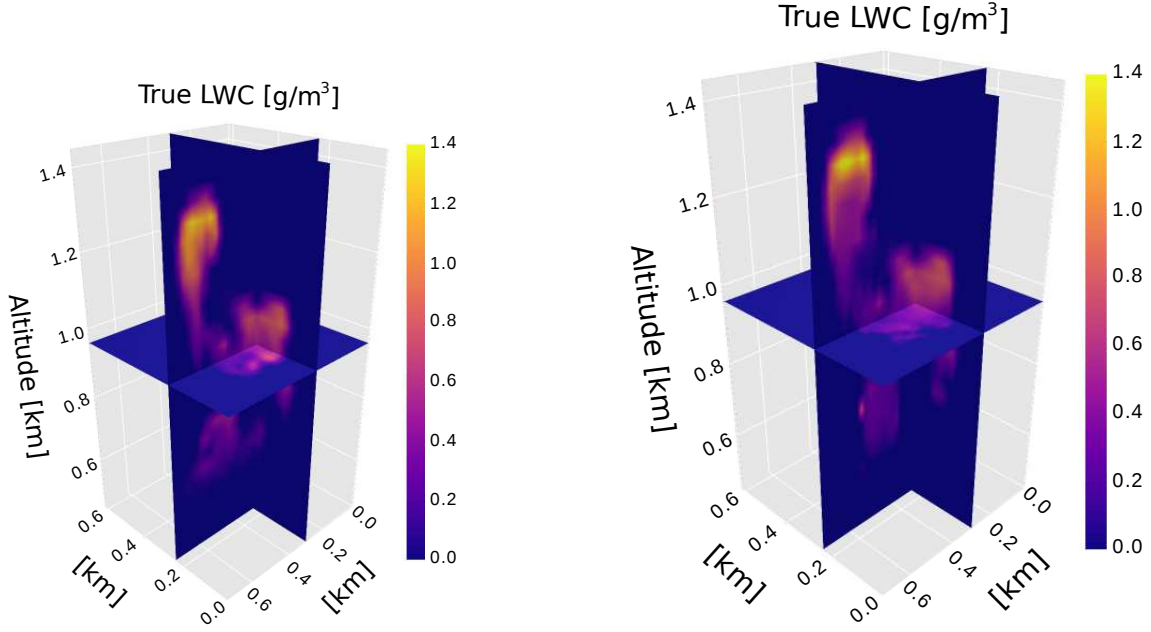
9

Figure 9: `Scene A` recovery results. [Left] Slices of the true cloud generated by LES. [Right] Slices of the cloud estimated tomographically using AirMSPI polarized bands.
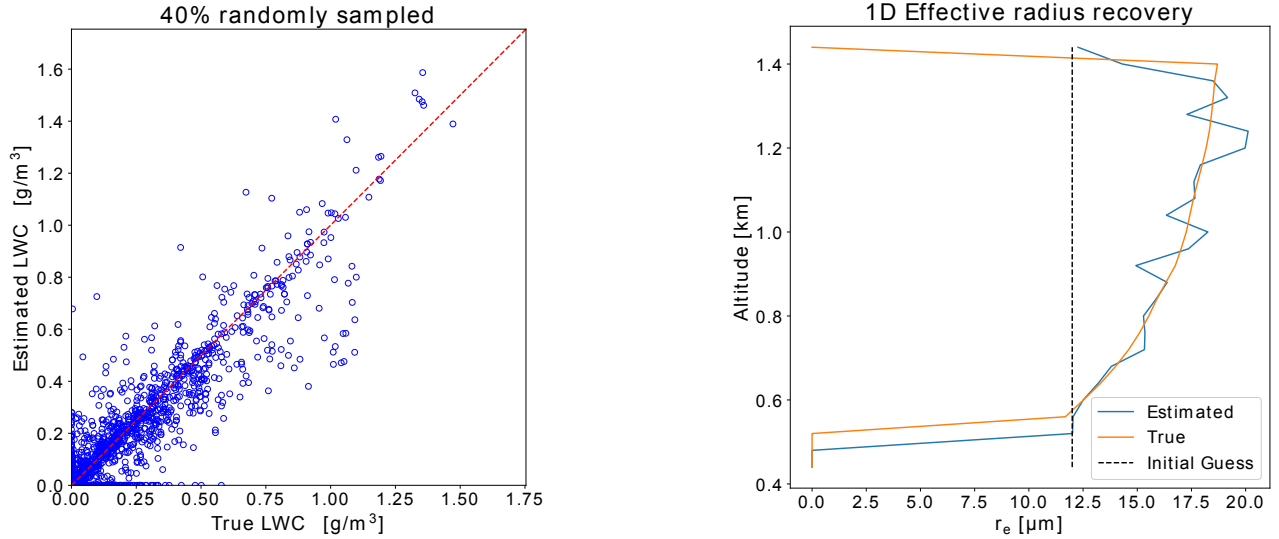

Figure 10: `Scene A` recovery results. [Left] Scatter plot of estimated vs. true LWC. The correlation coefficient is 0.94. [Right] recovery results of the 1D effective radius.

For quantitative assessment of the recovery, we use local mean error ϵ, and global bias measures[41] ϑ:

$$\epsilon_{\mathrm{LWC}} = \frac{\|\mathrm{L\hat{W}C} - \mathrm{LWC}\|_1}{\|\mathrm{LWC}\|_1}, \quad \vartheta_{\mathrm{LWC}} = \frac{\|\mathrm{L\hat{W}C}\|_1 - \|\mathrm{LWC}\|_1}{\|\mathrm{LWC}\|_1}, \quad \epsilon_{r_{\mathrm{e}}} = \frac{\|\hat{r_{\mathrm{e}}} - r_{\mathrm{e}}\|_1}{\|r_{\mathrm{e}}\|_1}. \tag{23}$$
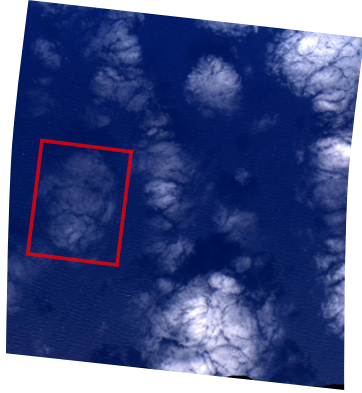
The quantitative error measures upon convergence for the two scenes are:

`Scene A:` $\epsilon_{r_e} \approx 11\%$, $\epsilon_{\mathrm{LWC}} \approx 30\%$, $\vartheta_{\mathrm{LWC}} \approx -4\%$,
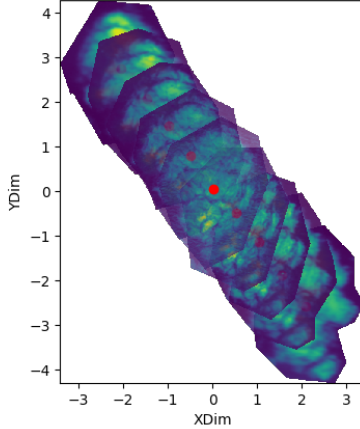
`Scene B:` $\epsilon_{r_e} \approx 13\%$, $\epsilon_{\mathrm{LWC}} \approx 29\%$, $\vartheta_{\mathrm{LWC}} \approx -5\%$.

Using a 2.50 GHz CPU, the recovery run-time of cloud properties in `Scenes A,B` was ~13 hours and ~10 days, respectively.
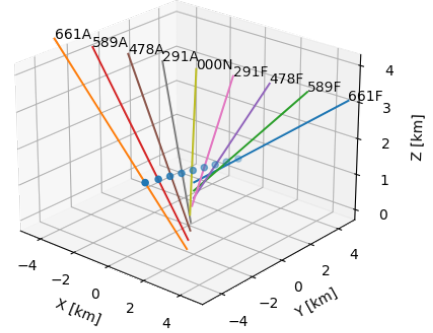
Figure 11: [Left] Nadir AirMSPI image where a relatively small cloud has been selected for tomographic reconstruction. [Middle] The cloud image center-of-mass (COM) is used to track the motion of the cloud during the overflight of the NASA ER-2. [Right] Linear motion of the cloud COM in 3D space is used to co-register the 9 AirMSPI images.

Multi-angular tomographic retrieval enables vertical resolution of the droplet effective radius. By contrast, a homogeneous droplet radius is typically retrieved by mono-angular observations fitted to a plane-parallel homogeneous cloud model. The retrieval errors of droplet radii in the demonstrations above are significantly smaller than retrieval errors of a homogeneous droplet radius. The latter can easily exceed 50% in similar conditions to our study, i.e, shallow cumuli and illumination conditions (see, e.g., Seethala[42]).

5. APPLICATION TO A REAL CLOUD

We conclude this investigation with a 3D microphysical tomography of a real cloud observed by AirMSPI on the NASA ER-2 platform ($\sim$20 km altitude) during the POlarimeter DEfinition EXperiment (PODEX) field campaign over the NE Pacific Ocean.[43] The data of interest was collected at (32N,123W) on 02/06/2013, and can be downloaded from here. Figure 11 shows the nadir view of the cloud scene and the selected cloud highlighted (left panel). Also displayed are the key 2D (middle panel) and 3D (right panel) co-registrations of the multi-angle imaging that factor in the motion of the cloud during the ER-2 overflight (20:24:16 to 20:31:33 GMT).

The number of $65{\times}65{\times}50$ [m^3] cells in the 3D grid for the RT is $[35{\times}45{\times}26] = 40{,}950$. The number of tomography unknowns for optimization is reduced by space-carving from $40{,}950{\times}2$ to $7{,}462{\times}2 = 14{,}924$. The optimization converges within 65 iterations, which takes 32 minutes on a standard (2.50 GHz CPU) Linux workstation. The Lambertian albedo for the ocean surface is set to 0.01.

Figure 12 displays, from left to right, the histogram of recovered LWC (above 0.001 g/m^3) across the 3D field, horizontal means and standard deviations of both LWC and r_e as functions of elevation (along with initial guesses), and the retrieved 2D cloud optical thickness map. As expected from Fig. 11 (left panel), optical thickness is small for clouds (i.e., $\lesssim$3). In the present absence of ground truth from in-situ probes on low-flying aircraft, there is no reason to dismiss these LWC and r_e retrievals. In contrast with the LES-based simulations from the previous Section, r_e can now vary across all the voxels, but still with a fixed and uniform $v_e = 0.1$. In that case, we can say that the retrieved LWC and r_e profiles point to a cloud that has passed its invigorating convective phase, that is, when one anticipates a linear increase in LWC and a weaker power-law increase in r_e with height above cloud base.

Lastly, we obtain the results of a simple cross-validation for the AirMSPI cloud tomography when we leave out of the retrieval one of the Stokes vector images, and then compare it with its prediction based on the recovered 3D LWC and r_e fields. This is done in Fig. 13 where we see particularly good agreement in the I component where the radiance levels are an order-of-magnitude larger than in its polarized counterparts. That is a typical situation outside of the cloud-bow and glory directions.
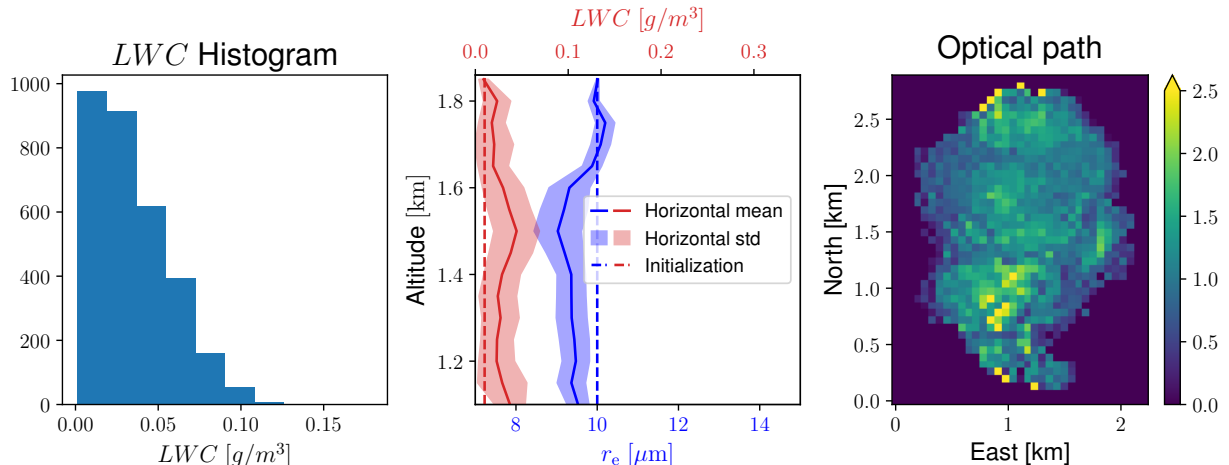
Figure 12: [Left] Following Yum et al.,[44] the recovered LWC is thresholded at 0.001 g/m^3 in this histogram. [Middle] The profiles of mean and standard deviation of both LWC and r_e are plotted along with the respective choices of initial guess. [Right] Vertically-integrated optical thickness from the recovered extinction mapped at the pixel scale.

6. SUMMARY & OUTLOOK

We derive a 3D tomography of cloud microphysics based on multi-view/multi-spectral polarimetric measurements of scattered sunlight. This novel type of tomography uses, for the first time, 3D polarized RT as the image formation model. We define a model-fitting error function and compute approximate gradients of this function to make the recovery tractable. Demonstrations are done on synthetic 3D clouds, based on a Large Eddy Simulation with the effective radius assumed to vary only vertically. The new cloud remote sensing capability is illustrated with airborne data acquired by AirMSPI during the PODEX field campaign.

Future work will address the extent to which polarimetric measurements penetrate the cloud and the relation between r_e in the *outer shell* and r_e in the cloud's *"veiled" core*, as defined by Forster et al.[45] Furthermore, we will relax the fixed v_e assumption used in the present demonstrations, and thus assess full microphysical retrieval capabilities of polarization measurements.

Lastly, we note that our atmospheric tomography approach herein can be adapted to aerosols, including dense plumes of wild fire smoke, volcanic ash, and dust. The only requirement, following directly from the forward image-formation model, is that pixels can be assumed internally uniform. This constraint is easily satisfied for airborne sensors, but problematic for space-based counterparts. Research is ongoing[45] about such adaptation for satellite data as can be obtained from the multi-view imaging from Multi-angle Imaging Spectro-Radiometer (MISR) on Terra and a SWIR view from the collocated MODIS sensor and, looking forward, from the CloudCT[8] nanosat constellation.
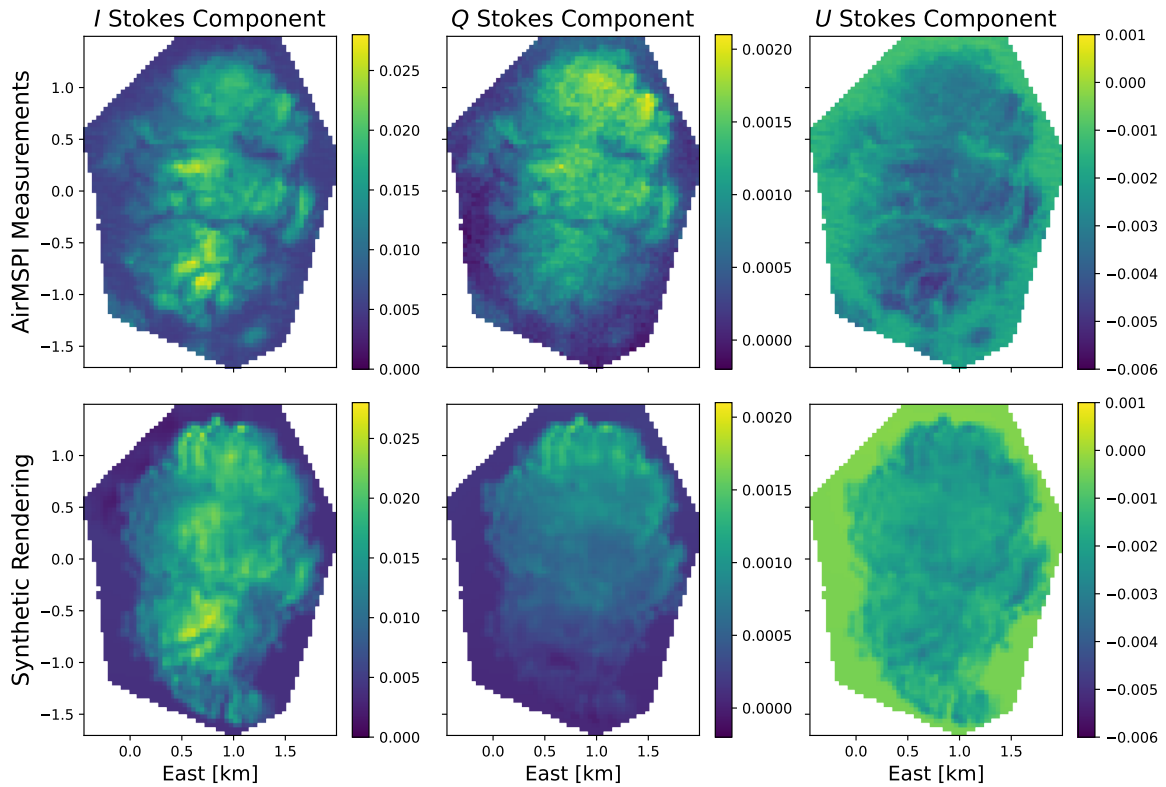
Acknowledgements

Figure 13: [Top row] 29.1°-aft AirMSPI measurements of Stokes vector components (I, Q, U), from left to right, that are *not* used in the tomography. [Bottom row] Same as top row, but rendered by vSHDOM using LWC and r_e fields recovered using the 8 other views and the prescribed $v_\mathrm{e} = 0.1$.

REFERENCES

[1] Trenberth, K. E., Fasullo, J. T., and Kiehl, J., "Earth's global energy budget," *Bulletin of the American Meteorological Society* **90**(3), 311–324 (2009).

[2] Boucher, O., Randall, D., Artaxo, P., Bretherton, C., Feingold, G., Forster, P., Kerminen, V.-M., Kondo, Y., Liao, H., Lohmann, U., et al., "Clouds and aerosols," in [*Climate Change 2013: The Physical Science Basis. Contribution of Working Group I to the Fifth Assessment Report of the Intergovernmental Panel on Climate Change*], 571–657, Cambridge University Press, Cambridge (UK) (2013).

[3] Rosenfeld, D. and Lensky, I. M., "Satellite-based insights into precipitation formation processes in continental and maritime convective clouds," *Bulletin of the American Meteorological Society* **79**(11), 2457–2476 (1998).

[4] Platnick, S., King, M., Ackerman, S., Menzel, W., Baum, B., Riedi, J., and Frey, R., "The MODIS cloud products: Algorithms and examples from Terra," *IEEE Trans. Geosci. Remote Sens.* **41**, 459–473 (2003).

[5] Marshak, A., Platnick, S., Várnai, T., Wen, G., and Cahalan, R. F., "Impact of three-dimensional radiative effects on satellite retrievals of cloud droplet sizes," *Journal of Geophysical Research: Atmospheres* **111**(D9), doi:10.1029/2005JD006686 (2006).

[6] Cho, H.-M., Zhang, Z., Meyer, K., Lebsock, M., Platnick, S., Ackerman, A. S., Di Girolamo, L., C.-Labonnote, L., Cornet, C., Riedi, J., et al., "Frequency and causes of failed modis cloud property retrievals for liquid phase clouds over global oceans," *Journal of Geophysical Research: Atmospheres* **120**(9), 4132–4154 (2015).

[7] National Academies of Sciences, Engineering, and Medicine, [*Thriving on Our Changing Planet: A Decadal Strategy for Earth Observation from Space*], The National Academies Press, Washington, DC, USA (2018).

[8] Schilling, K., Schechner, Y. Y., and Koren, I., "CloudCT - computed tomography of clouds by a small satellite formation," *IAA Symposium on Small Satellites for Earth Observation* , IAC–19–D1.6.3 (2019).

[9] Nakajima, T. and King, M. D., "Determination of the optical thickness and effective particle radius of clouds from reflected solar radiation measurements. Part I: Theory," *Journal of the Atmospheric Sciences* **47**(15), 1878–1893 (1990).

[10] Deschamps, P.-Y., Bréon, F.-M., Leroy, M., Podaire, A., Bricaud, A., Buriez, J.-C., and Seze, G., "The POLDER mission: Instrument characteristics and scientific objectives," *IEEE Transactions on Geoscience and Remote Sensing* **32**(3), 598–615 (1994).

[11] Bréon, F.-M. and Goloub, P., "Cloud droplet effective radius from spaceborne polarization measurements," *Geophysical Research Letters* **25**(11), 1879–1882 (1998).

[12] Kalashnikova, O. V., Garay, M. J., Davis, A. B., Diner, D. J., and Martonchik, J. V., "Sensitivity of multi-angle photo-polarimetry to vertical layering and mixing of absorbing aerosols: Quantifying measurement uncertainties," *Journal of Quantitative Spectroscopy and Radiative Transfer* **112**(13), 2149–2163 (2011).

[13] Lukashin, C., Wielicki, B. A., Young, D. F., Thome, K., Jin, Z., and Sun, W., "Uncertainty estimates for imager reference inter-calibration with CLARREO reflected solar spectrometer," *IEEE Transactions on Geoscience and Remote Sensing* **51**(3), 1425–1436 (2013).

[14] Diner, D., Xu, F., Garay, M., Martonchik, J., Rheingans, B., Geier, S., Davis, A., Hancock, B., Jovanovic, V., Bull, M., et al., "The Airborne Multiangle SpectroPolarimetric Imager (AirMSPI): A new tool for aerosol and cloud remote sensing," *Atmospheric Measurement Techniques* **6**(8), 2007–2025 (2013).

[15] Diner, D. J., Boland, S. W., Brauer, M., Bruegge, C., Burke, K. A., Chipman, R., Di Girolamo, L., Garay, M. J., Hasheminassab, S., Hyer, E., et al., "Advances in multiangle satellite remote sensing of speciated airborne particulate matter and association with adverse health effects: From MISR to MAIA," *Journal of Applied Remote Sensing* **12**(4), 042603 (2018).

[16] Emde, C., Barlakas, V., Cornet, C., Evans, F., Korkin, S., Ota, Y., Labonnote, L. C., Lyapustin, A., Macke, A., Mayer, B., et al., "IPRT polarized radiative transfer model intercomparison project – Phase A," *Journal of Quantitative Spectroscopy and Radiative Transfer* **164**, 8–36 (2015).

[17] Emde, C., Barlakas, V., Cornet, C., Evans, F., Wang, Z., Labonotte, L. C., Macke, A., Mayer, B., and Wendisch, M., "IPRT polarized radiative transfer model intercomparison project – three-dimensional test cases (Phase B)," *Journal of Quantitative Spectroscopy and Radiative Transfer* **209**, 19–44 (2018).

[18] Levis, A., Schechner, Y. Y., Davis, A. B., and Loveridge, J., "Multi-view polarimetric scattering cloud tomography and retrieval of droplet size," *Remote Sensing* **12**(17), 2831 (2020).

[19] Kak, A. and Slaney, M., [*Principles of Computerized Tomographic Imaging IEEE Press*], IEEE Press, Piscataway, NJ, USA (1988).

[20] Gordon, R., Bender, R., and Herman, G. T., "Algebraic reconstruction techniques (ART) for three-dimensional electron microscopy and X-ray photography," *Journal of Theoretical Biology* **29**(3), 471–481 (1970).

[21] Arridge, S. R., "Optical tomography in medical imaging," *Inverse Problems* **15**(2), R41 (1999).

[22] Boas, D. A., Brooks, D. H., Miller, E. L., DiMarzio, C. A., Kilmer, M., Gaudette, R. J., and Zhang, Q., "Imaging the body with diffuse optical tomography," *IEEE Signal Processing Magazine* **18**(6), 57–75 (2001).

[23] Arridge, S. R. and Schotland, J. C., "Optical tomography: Forward and inverse problems," *Inverse Problems* **25**(12), 123010 (2009).

[24] Che, C., Luan, F., Zhao, S., Bala, K., and Gkioulekas, I., "Inverse transport networks," *arXiv preprint arXiv:1809.10820* (2018).

[25] Evans, K. F., "The spherical harmonics discrete ordinate method for three-dimensional atmospheric radiative transfer," *Journal of the Atmospheric Sciences* **55**(3), 429–446 (1998).

[26] Doicu, A., Efremenko, D., and Trautmann, T., "A multi-dimensional vector spherical harmonics discrete ordinate method for atmospheric radiative transfer," *Journal of Quantitative Spectroscopy and Radiative Transfer* **118**, 121–131 (2013).

[27] Levis, A., Schechner, Y. Y., Aides, A., and Davis, A. B., "Airborne three-dimensional cloud tomography," in [*Proceedings of the IEEE International Conference on Computer Vision*], 3379–3387, Proceedings of the IEEE International Conference on Computer Vision (2015).

[28] Holodovsky, V., Schechner, Y. Y., Levin, A., Levis, A., and Aides, A., "In-situ multi-view multi-scattering stochastic tomography," in [*2016 IEEE International Conference on Computational Photography (ICCP 2016)*], 1–12, 2016 IEEE International Conference on Computational Photography (2016).

[29] Levis, A., Schechner, Y. Y., and Davis, A. B., "Multiple-scattering microphysics tomography," in [*Proceedings of the IEEE Conference on Computer Vision and Pattern Recognition*], 6740–6749, Proceedings of the IEEE Conference on Computer Vision and Pattern Recognition (2017).

[30] Martin, W., Cairns, B., and Bal, G., "Adjoint methods for adjusting three-dimensional atmosphere and surface properties to fit multi-angle/multi-pixel polarimetric measurements," *Journal of Quantitative Spectroscopy and Radiative Transfer* **144**, 68–85 (2014).

[31] Martin, W. G. and Hasekamp, O. P., "A demonstration of adjoint methods for multi-dimensional remote sensing of the atmosphere and surface," *Journal of Quantitative Spectroscopy and Radiative Transfer* **204**, 215 – 231 (2018).

[32] Hansen, J. E., "Multiple scattering of polarized light in planetary atmospheres, Part II. Sunlight reflected by terrestrial water clouds," *Journal of the Atmospheric Sciences* **28**(8), 1400–1426 (1971).

[33] Chylek, P., "Extinction and liquid water content of fogs and clouds," *Journal of the Atmospheric Sciences* **35**(2), 296–300 (1978).

[34] Chandrasekhar, S., [*Radiative Transfer*], Oxford University Press, Oxford (UK) (1950). [reprinted by Dover Publications, New York (NY), 1960, and by Courier Corporation, 2013].

[35] Bohren, C. F. and Huffman, D. R., [*Absorption and Scattering of Light by Small Particles*], John Wiley & Sons (2008).

[36] Mayer, B., "Radiative transfer in the cloudy atmosphere," in [*EPJ Web of Conferences*], **1**, 75–99, EPJ Web of Conferences, EDP Sciences (2009).

[37] Anderson, G. P., Clough, S. A., Kneizys, F., Chetwynd, J. H., and Shettle, E. P., "AFGL atmospheric constituent profiles (0.120 km)," tech. rep., Air Force Geophysics Lab (1986).

[38] Matheou, G. and Chung, D., "Large-eddy simulation of stratified turbulence. Part 2: Application of the stretched-vortex model to the atmospheric boundary layer," *Journal of the Atmospheric Sciences* **71**(12), 4439–4460 (2014).

[39] Yau, M. K. and Rogers, R. R., [*A short course in cloud physics*], Elsevier (1996).

[40] van Harten, G., Diner, D. J., Daugherty, B. J., Rheingans, B. E., Bull, M. A., Seidel, F. C., Chipman, R. A., Cairns, B., Wasilewski, A. P., and Knobelspiesse, K. D., "Calibration and validation of Airborne Multiangle SpectroPolarimetric Imager (AirMSPI) polarization measurements," *Applied Optics* **57**(16), 4499–4513 (2018).

[41] Aides, A., Schechner, Y. Y., Holodovsky, V., Garay, M. J., and Davis, A. B., "Multi sky-view 3D aerosol distribution recovery," *Optics Express* **21**(22), 25820–25833 (2013).

[42] Seethala, C., *Evaluating the state-of-the-art of and errors in 1D satellite cloud liquid water path retrievals with large eddy simulations and realistic radiative transfer models*, PhD thesis, University of Hamburg, Hamburg (Germany) (2012).

[43] Diner, D. J., Garay, M. J., Kalashnikova, O. V., Rheingans, B. E., Geier, S., Bull, M. A., Jovanovic, V. M., Xu, F., Bruegge, C. J., Davis, A., Crabtree, K., and Chipman, R. A., "Airborne multiangle spectropolarimetric imager (AirMSPI) observations over California during NASA's polarimeter definition experiment (PODEX)," in [*Polarization Science and Remote Sensing VI*], Shaw, J. A. and LeMaster, D. A., eds., **8873**, 88 – 97, International Society for Optics and Photonics, SPIE (2013).

[44] Yum, S. S., Wang, J., Liu, Y., Senum, G., Springston, S., McGraw, R., and Yeom, J. M., "Cloud microphysical relationships and their implication on entrainment and mixing mechanism for the stratocumulus clouds measured during the vocals project," *Journal of Geophysical Research: Atmospheres* **120**(10), 5047–5069 (2015).

[45] Forster, L., Davis, A. B., Diner, D. J., and Mayer, B., "Toward cloud tomography from space using MISR and MODIS: Locating the "veiled core" in opaque convective clouds," *Journal of the Atmospheric Sciences* **78**(1), 155–166 (2021).